crystals

MDPI

Article

Photoluminescence of the Eu^{3+}-Activated $Y_xLu_{1-x}NbO_4$ (x = 0, 0.25, 0.5, 0.75, 1) Solid-Solution Phosphors

Milica Sekulić, Tatjana Dramićanin, Aleksandar Ćirić, Ljubica Đačanin Far, Miroslav D. Dramićanin and Vesna Đorđević *

Center of Excellence for Photoconversion, Vinča Institute of Nuclear Sciences—National Institute of the Republic of Serbia, University of Belgrade, P.O. Box 522 Belgrade, Serbia; milicasekulic88@gmail.com (M.S.); tatjana@vin.bg.ac.rs (T.D.); aleksandar.ciric@ff.bg.ac.rs (A.Ć.); ljubica.far@vin.bg.ac.rs (L.Đ.F.); dramican@vinca.rs (M.D.D.)

* Correspondence: vesipka@vinca.rs; Tel.: +381-11-340-8191

Abstract: Eu^{3+}-doped $Y_xLu_{1-x}NbO_4$ (x = 0, 0.25, 0.5, 0.75, 1) were prepared by the solid-state reaction method. $YNbO_4$:Eu^{3+} and $LuNbO_4$:Eu^{3+} crystallize as beta-Fergusonite (SG no. 15) in 1–10 μm diameter particles. Photoluminescence emission spectra show a slight linear variation of emission energies and intensities with the solid-solution composition in terms of Y/Lu content. The energy difference between Stark sublevels of $^5D_0 \rightarrow {}^7F_1$ emission increases, while the asymmetry ratio decreases with the composition. From the dispersion relations of pure $YNbO_4$ and $LuNbO_4$, the refractive index values for each concentration and emission wavelength are estimated. The Ω_2 Judd–Ofelt parameter shows a linear increase from 6.75 to 7.48 × 10^{-20} cm^2 from x = 0 to 1, respectively, and Ω_4 from 2.69 to 2.95 × 10^{-20} cm^2. The lowest non-radiative deexcitation rate was observed with x = 1, and thus $LuNbO_4$:Eu^{3+} is more efficient phosphor than $YNbO_4$:Eu^{3+}.

Keywords: phosphor; Eu^{3+}; niobates; Judd-Ofelt; quantum efficiency; refractive index

Citation: Sekulić, M.; Dramićanin, T.; Ćirić, A.; Đačanin Far, L.; Dramićanin, M.D.; Đorđević, V. Photoluminescence of the Eu^{3+}-Activated $Y_xLu_{1-x}NbO_4$ (x = 0, 0.25, 0.5, 0.75, 1) Solid-Solution Phosphors. *Crystals* **2022**, *12*, 427. https://doi.org/10.3390/cryst12030427

Academic Editors: Alessandra Toncelli and Željka Antić

Received: 18 February 2022
Accepted: 15 March 2022
Published: 19 March 2022

1. Introduction

Phosphors designed with rare earth (RE)-activated compounds are a continuously rising research topic in both basic and applied science. Materials containing the trivalent europium ion (Eu^{3+}) are well known for their strong luminescence in the orange/red spectral region, making them suitable for use in artificial lights, display devices, luminescent sensing, and biomedical research, among other applications [1–4]. In addition, the Eu^{3+} ion is a truly unique spectroscopic probe from a theoretical point of view. Because the 4*f* shell of Eu^{3+} has an even number of electrons ([Xe]$4f^6$), the ion exhibits a non-degenerated ground ($^7F_0$) and excited ($^5D_0$) energy states, as well as non-overlapping $^{2S+1}L_J$ multiplets, resulting in emission spectra that are predictably dependent on the host material site symmetry. The energy level structure, the intensities of the *f*-*f* transitions (including the Judd–Ofelt theory), and the decay times of the excited states allow the Eu^{3+} ion to be used as a spectroscopic probe [5–8].

Compounds with the ABO_4 composition (A = RE; B = P, V, Nb) are suggested to be excellent hosts for luminescent materials in the vast field of phosphors [9–11] due to the coupling between rare-earth (RE^{3+}) ions and the $BO_4{}^{3-}$ group. RE-Niobates ($RENbO_4$) have long been known, but have received far less attention than vanadates or phosphates. They are chemically stable and have good dielectric properties, as well as ion and proton conductivities [12–15]. They have been prepared as single crystals [16,17], thin films [18], and in crystalline power form [19,20] for a variety of potential applications, primarily as optical hosts. Under UV or x-ray excitation, $YNbO_4$ is a self-activated phosphor with a broad and strong emission band in the blue spectral region around 400 nm (associated with $NbO_4{}^{3-}$ groups from the host crystalline lattice) [21,22]. RE-Niobates' luminescent properties can be altered by doping with various rare-earth ions. Emission has been

observed from: Tm^{3+}, Tb^{3+}, Dy^{3+}, Sm^{3+}, Er^{3+}, Nd^{3+} [23–28], and Eu^{3+} [20,29]. Recent applications of RE-doped niobates involved luminescent temperature sensors [27,30].

The $RENbO_4$ structure type has a more complex profile than the $REVO_4$ materials, which always occurs in the typical tetragonal zircon structure type. $YNbO_4$ was originally thought to be the parent material of the $RENbO_4$ group, like the natural mineral fergusonite, leading to the classification of the material as a tetragonal phase with a scheelite (I41/a) structure [31]. However, there are two major crystalline forms of $RENbO_4$. One is the low-temperature M-phase isostructure with a monoclinic form of the fergusonite, and the other is the high-temperature T-phase corresponding to the tetragonal scheelite. Between 500 and 850 °C, the reversible transition between two phases, monoclinic and tetragonal, occurs [32]. Subsequent research revealed that the low-temperature phase, monoclinic beta-Fergusonite structure can be described by the space group I-centered (I12/a1) or C-centered (C12/c1), as the I2/a space group is a non-standard setting of C2/c (SG no. 15) [33–35]. In both settings, Y is surrounded by 8 oxygens in a large, low-symmetry YO_8 octahedron [34]. When other rare earth ions, such as Eu^{3+}, occupy the Y site, the tilting of adjacent NbO_4 and NbO_6 polyhedra is expected to influence the luminescence properties of the dopant.

In this study, we wanted to investigate the effect of different ionic radii of RE^{3+} ions on the photoluminescence of the Eu^{3+}-activated niobate host. We prepared a set of five Eu-doped $Y_xLu_{1-x}NbO_4$:Eu samples (x = 0, 0.25, 0.5, 0.75, and 1) with a fixed Eu concentration (5%) to investigate the influence of the Y to Lu ratio in the host niobate material on Eu^{3+} luminescence features. In that sense, the crystal field splitting of $^7F_1$ manifold, R intensity ratio and Judd–Ofelt parameters were determined. The application of Judd–Ofelt theory was explained, and the difference in the refractive index of the materials was considered.

2. Materials and Methods

The set of five samples, Eu-doped $Y_xLu_{1-x}NbO_4$:Eu^{3+} (x = 0, 0.25, 0.5, 0.75, and 1), were prepared by the solid-state reaction method. In the stoichiometric amounts of starting materials, Yttirium(III) oxide (Y_2O_3 Alfa Aesar, 99.9%), Lutetium(III) oxide (Lu_2O_3, Alfa Aeser 99.9%), and Niobium(V) oxide (Nb_2O_5 Alfa Aesar, 99.5%) were mixed with Europium oxide (Eu_2O_3 Alfa Aesar, 99.9%) added in order for Y or Lu to reach 95% (i.e., $Y_{0.95}Eu_{0.05}NbO_4$). With the addition of sodium sulphate decahydrate (Na_2SO_4 x $10H_2O$, Alfa Aesar, 99%) as flux and small amount of ethanol, the mixtures were homogenized in a ball mill (BM500, Anton Paar) for several hours. The dried mixture was pre-sintered at 800 °C for 2 h, then sintered at 1450 °C for 8 h and allowed to cool to room temperature. Such obtained powders or pellets prepared from the powder under a load of 5×10^8 Pa were used for measurements.

X-ray diffraction measurements were performed with a Rigaku SmartLab diffractometer (Tokyo, Japan) using Cu Kα radiation (30 mA, 40 kV) measured in the 2θ range from 10° to 90°. The built-in package software was used to obtain relevant structural analysis results (crystal coherence size, microstrain values, unit cell parameters, and data fit parameters). A Mira3 Tescan field emission scanning electron microscope (FE-SEM) (Brno, Czech Republic) was used for microstructural characterization, operated at 20 keV and 5.00 kx magnification. Photoluminescence excitation spectra were measured by a Horiba Jobin Yvon Fluorolog FL3-221 spectrofluorometer (Palaiseau, France) equipped with a 450 W Xenon lamp, TBX-04-D PMT detector and a double-grating monochromator with 1200 g/mm. The excitations were performed by monitoring the emission maxima at 612 nm. Lifetime measurements were performed using the same instrument equipped with a xenon–mercury pulsed lamp. Photoluminescence emission spectra were recorded by a high-resolution spectrograph (FHR 1000) (Palaiseau, France) equipped with a Horiba Jobin–Yvon Intensified Charge Coupled Device–ICCD detector and selectable diffraction gratings of 300 and 1800 g/mm. Samples were excited by a 365 nm LED (Ocean Optics) and driven by an Ocean Insight LDC-1C controller.

3. Results

3.1. Crystal Structure and Morphology

X-ray diffraction measurements confirmed that $YNbO_4$:Eu crystallizes in a monoclinic Fergusonite-beta-(Y) structure that can be best fitted with the C2/c space group corresponding to pure $YNbO_4$ ICDD No. 01-083-1319, as can be seen in Figure 1 [36]. The isostructural incorporation of a bigger Eu^{3+} (r_{VIII} = 1.066 Å) ion instead of a Y^{3+} (r_{VIII} = 1.019 Å) ion of YO_8 dodecahedra results in a small maximum shift of approximately 0.03° to the lower 2θ values [37]. X-ray diffraction measurements confirmed that $LuNbO_4$:Eu^{3+} crystallizes in a monoclinic Fergusonite-beta-(Lu) structure that can be best fitted with the I2/a space group corresponding to pure $LuNbO_4$ ICDD No. 01-074-6538, as can be seen in Figure 1 [35]. A slight peak position shift of around 0.1° to the lower 2θ values is also observed, resulting from the isostructural incorporation of a larger Eu^{3+} (r_{VIII} = 1.066 Å) ion into the Lu^{3+} (r_{VIII} = 0.977 Å) position of LuO_8 dodecahedra [36].

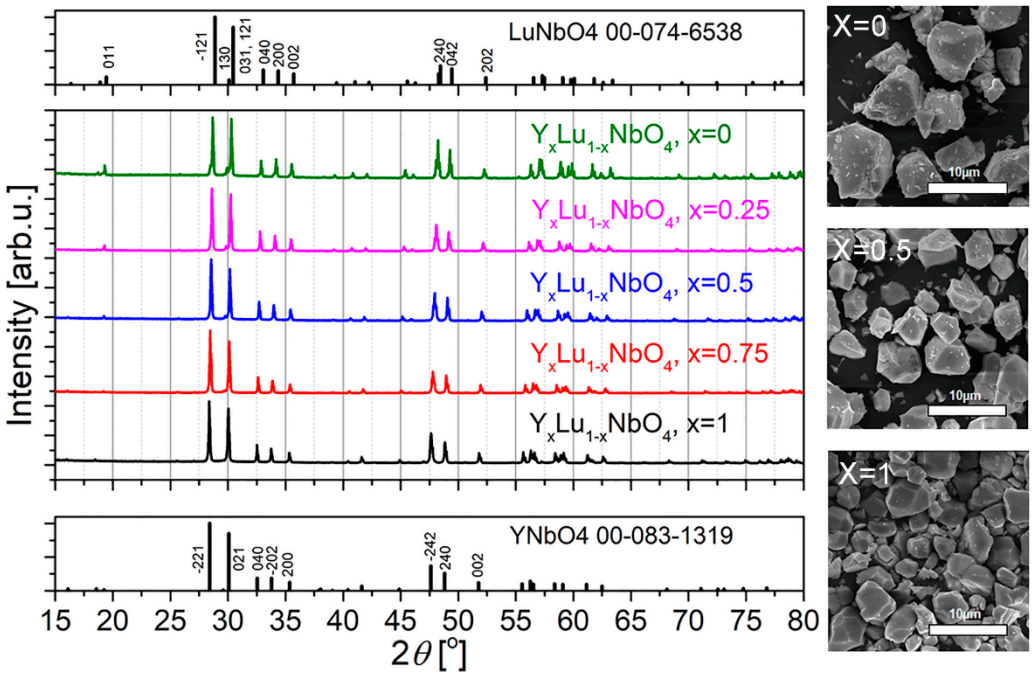

Figure 1. Comparison of the powder x-ray diffraction patterns of the $Y_xLu_{1x}NbO_4$:5%Eu (x = 0, 0.25, 0.5, 0.75, 1) samples with representative SEM images of $Y_xLu_{1-x}NbO_4$:5%Eu (x = 0, 0.5, 1) with a 10-micron bar.

Table 1 shows the relevant structural characteristics for both final compositions of $Y_xLu_{1-x}NbO_4$:Eu^{3+} (x = 0 and 1), determined by Rietveld refinement of the experimental data derived from Rigaku SmartLab built-in package software. The $YNbO_4$:Eu^{3+} (x = 1) parameters are refined to the C2/c space group, with a higher value of parameter **a** of the unit cell around 7.63 Å and a higher **β** of 138.44°, whereas $LuNbO_4$:Eu^{3+} (x = 0) parameters are refined to the I2/a space group, with a lower value of parameter **a** of the unit cell of around 5.24 Å and a lower **β** of 94.43°. Both samples have crystallite sizes of roughly 50 ± 3 nm and low strain values. The SEM images of $Y_xLu_{1-x}NbO_4$:5%Eu (x = 0, 0.5, 1) materials presented in Figure 1 show irregularly shaped particles ranging in size from 1 to 10 microns. The $YNbO_4$:5%Eu material comprises a higher proportion of smaller, densely packed particles, whereas the particles in the $LuNbO_4$:5%Eu material are larger and less densely packed.

Table 1. Structural parameters obtained by Rietveld refinement of XRD data for $YNbO_4$:Eu^{3+} according to ICDD 01-083-1319, and for $LuNbO_4$:Eu^{3+} according to ICDD 01-074-6538.

Ref. Parameters	$YNbO_4$:Eu^{3+} (C2/c)	$LuNbO_4$:Eu^{3+} (I2/a)
Crystallite size (Å)	533(6)	479(6)
Strain (%)	0.08(2)	0.11(2)
a (Å)	7.62775(17)	5.23879(13)
b (Å)	10.9636(3)	10.8447(3)
c (Å)	5.30476(15)	5.04724(12)
α (°)	90	90
β (°)	138.4389(11)	94.4267(13)
γ (°)	90	90
Rwp [1]	10.28%	10.25%
Rp [2]	6.30%	6.55%
Re [3]	3.23%	3.32%
GOF [4]	3.1833	3.0895

[1] Rwp—regression sum of weighted squared errors of fit; [2] Rp—regression sum of relative squared errors of fit; [3] Re—regression sum of relative errors of fit; [4] GOF—goodness of fit parameter.

3.2. Photoluminescence

The luminescence excitation and emission spectra of the Eu^{3+} ($4f^6$) ion in $Y_xLu_{1-x}NbO_4$ (x = 0, 0.25, 0.5, 0.75, 1) hosts clearly show characteristic *f-f* transitions, as shown in Figure 2. The excitation spectra of all samples, observed in Figure 2a, as recorded at λem = 612 nm, show several dominant excitation bands centered at around 540 nm ($^7F_1 \rightarrow {}^5D_1$), 529 nm ($^7F_0 \rightarrow {}^5D_1$), 466 nm ($^7F_0 \rightarrow {}^5D_0$), 393 nm ($^7F_0 \rightarrow 5L_6$), and 365 nm ($^7F_0 \rightarrow {}^5D_4$). The emission spectra of all samples recorded with λexc = 365 nm excitation are presented in Figure 2b. Following the $^7F_0 \rightarrow {}^5D_4$ excitation, the electrons non-radiatively deexcite to the long-lived $^5D_0$ level, from where the radiative relaxation occurs to the ^7F_J ground multiplet. In the recorded region, five dominant emission bands from the $^5D_0$ level are centered at 595 nm ($^5D_0 \rightarrow {}^7F_1$), 612 nm ($^5D_0 \rightarrow {}^7F_2$), 655 nm ($^5D_0 \rightarrow {}^7F_3$), 710 nm ($^5D_0 \rightarrow {}^7F_4$), and 745 nm ($^5D_0 \rightarrow {}^7F_5$). The possible $^5D_0 \rightarrow {}^7F_6$ cannot be recorded by the used experimental setup. As is obvious from Figure 2, the luminescences in all the samples show overlapping bands characteristic for the Eu^{3+} ion. The Stark level energies calculated from the recorded excitation and emission spectra are presented in Table 2.

The intensity of the Eu^{3+} $^5D_0 \rightarrow {}^7F_2$ ($\Delta J = 2$) forced electric dipole transition is hypersensitive since it is strongly dependent on the coordinating polyhedron local site symmetry. Given that the environment of Eu^{3+} ion is a (Y,Lu)O_8 dodecahedron in all samples, small changes can be expected because of the variation of ion positions governed by the different ionic radii of Y and Lu ions [36].

The intensity of the parity-allowed Eu^{3+} $^5D_0 \rightarrow {}^7F_1$ ($\Delta J = 1$) magnetic dipole transition is considered as independent to the local symmetry; however, maximum splitting of the $^7F_1$ manifold of the Eu^{3+} ion is a function of the host [38]. To observe the influence of the host on the $^7F_1$ manifold, additional measurements were performed using a 1800 g/mm diffraction grating monochromator. To precisely determine the positions of all three maxima, a deconvolution is applied, as presented in Figure 2c.

The positions (Peak energies [cm^{-1}]) of the characteristic emission peak maxima of $Y_xLu_{1-x}NbO_4$:Eu (x = 0, 0.25, 0.5, 0.75, 1) are presented in Figure 3a. As can be seen, only small differences of around 10–20 cm^{-1} are determined, given the similarity of the Eu^{3+} ion local environment. Trends of maximum ΔE splitting, the Stark splitting of $^7F_1$ manifold, and the asymmetry ratio R corresponding to the Y/Lu content are presented in Figure 3b. As is evident, ΔE increases linearly with the increase of the x value (increase in Y content). For the same site symmetry and coordination number, the positions of the Stark levels of emissions originating from the $^5D_0$ level of Eu^{3+} depend on the covalency of the metal-ligand bond [39].

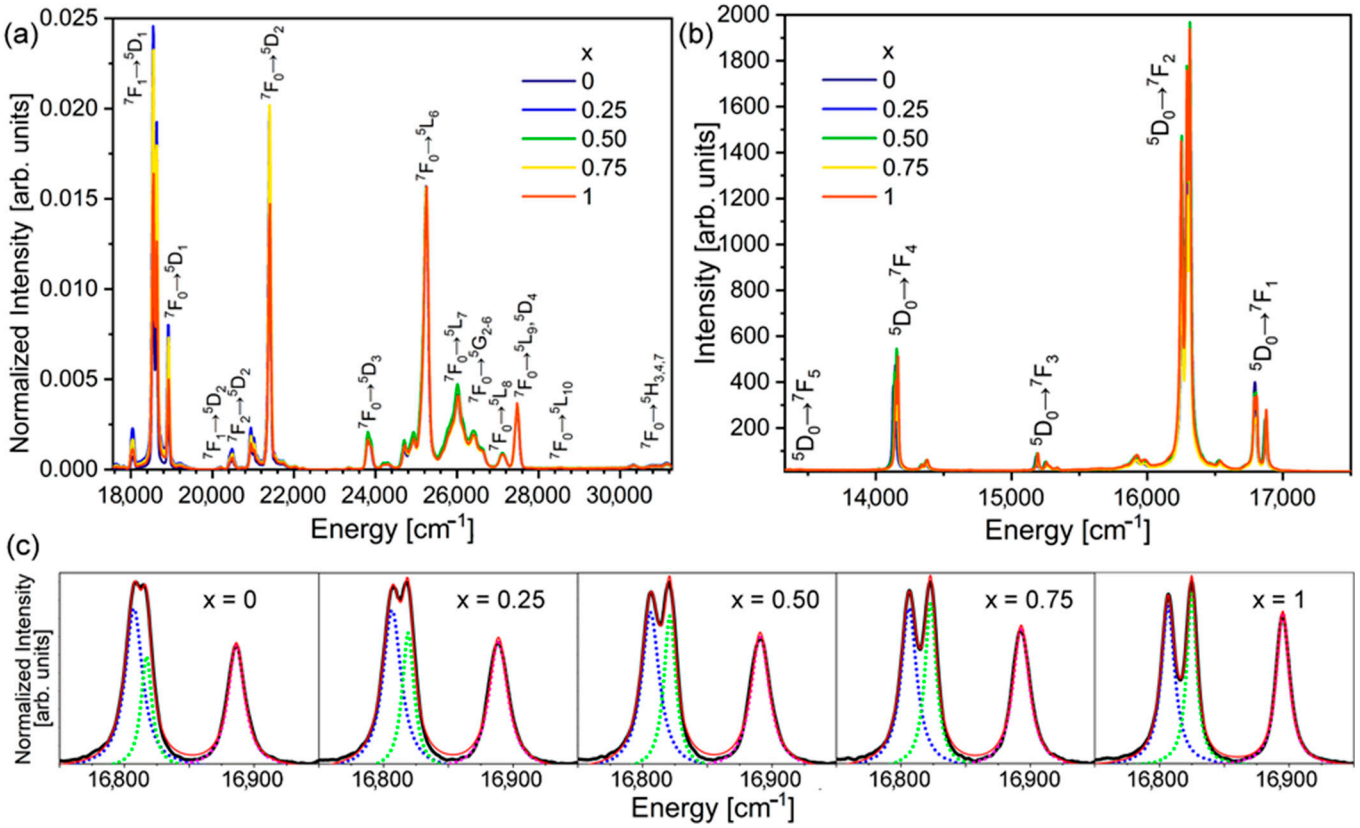

Figure 2. Luminescence spectra of $Y_xLu_{1-x}NbO_4:Eu^{3+}$ (x = 0, 0.25, 0.5, 0.75, 1): (**a**) Excitation recorded by monitoring 612 nm normalized to $^7F_0 \rightarrow {}^5L_6$; (**b**) Emission spectra of under 365 nm excitation and recorded with 300 g/mm, (**c**) Deconvolution of $^5D_0 \rightarrow {}^7F_1$ peaks recorded under 1800 g/mm diffraction grating.

Table 2. Calculated energy of Stark levels $Y_{0.5}Lu_{0.5}NbO_4$:5%Eu.

Level	Observed Energy [cm^{-1}]
$^7F_0$	0
$^7F_1$	369
$^7F_2$	1200
$^7F_3$	1960
$^7F_4$	2999
$^7F_5$	3799
$^7F_6$	N/A
$^5D_0$	17,204
$^5D_1$	18,921
$^5D_2$	21,402
$^5D_3$	23,810
$^5L_6$	25,253
$^5L_7$	26,008
$^5G_{2–6}$	26,420
$^5L_8$	27,100
$^5D_4 + {}^5L_9$	27,473
$^5L_{10}$	28,531
$^5H_{3,4,7}$	30,722

The asymmetry ratio R, which is the ratio of the two characteristic transitions, is frequently used to obtain information on the local site symmetry. As the ratio can be

influenced by the refractive index (n) of the host, experimental R values can be corrected for n using the following equation [40]:

$$R_{corr} = \left[\frac{9n^2}{(n^2+2)^2}\right]\frac{I(5_{D_0} - 7_{F_2})}{I(5_{D_0} - 7_{F_1})}. \quad (1)$$

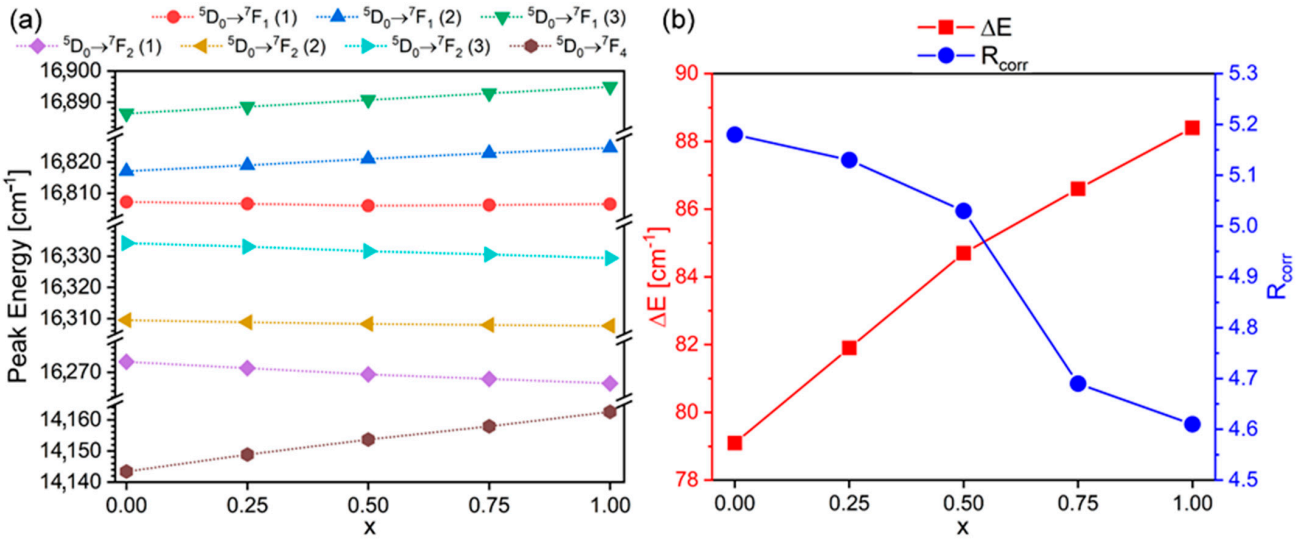

Figure 3. (**a**) Positions of the emission peak maxima of $Y_xLu_{1-x}NbO_4$:Eu^{3+} (x = 0, 0.25, 0.5, 0.75, 1); (**b**) Energy difference (ΔE) between $^5D_0 \rightarrow ^7F_1$ (1) and (3), and corrected asymmetry ratio (R_{corr}).

Starting n values for $LuNbO_4$ and $YNbO_4$ were obtained from Ref. [10]. The refractive index values for the other hosts were then calculated by approximation: $n(Y_xLu_{1-x}NbO_4) = x \cdot n(YNbO_4) + (1-x) \cdot n(LuNbO_4)$; and they are given in Figure 4. Characteristic n values at different wavelengths are clearly marked in Figure 4, and they are used for further Judd–Ofelt calculations.

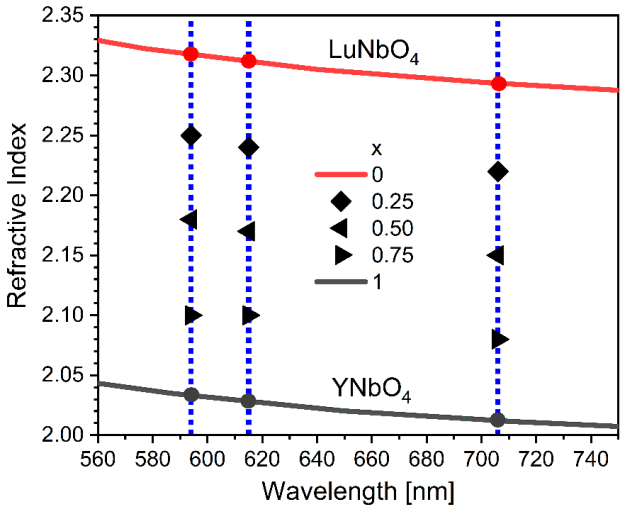

Figure 4. The calculated refractive index values for $Y_xLu_{1-x}NbO_4$ (x = 0, 0.25, 0.5, 0.75, 1).

3.3. Judd–Ofelt Analysis

Eu^{3+} is the only ion with pure magnetic dipole transitions, $^5D_0 \rightarrow ^7F_1$ and $^5D_1 \rightarrow ^7F_0$, allowing for the self-referenced Judd–Ofelt analysis from the single emission spectrum [5,6,41]. As the magnetic dipole transition strengths are independent of the host matrix, the radiative transition probability of the magnetic dipole transition (*MD*) can be used for calibration

of the spectrum [42]. Then, the Judd–Ofelt parameters can be estimated from the single emission spectrum (without the traditionally used fitting procedure [43,44]), directly from the relation [45,46]:

$$\Omega_\lambda \left[\mathrm{cm}^2\right] = \frac{4.135 \times 10^{-23}}{U^\lambda} \left(\frac{\nu_{MD}}{\nu_\lambda}\right)^3 \frac{9n_{MD}^3}{n_\lambda \left(n_\lambda^2+2\right)^2} \frac{I_\lambda}{I_{MD}}, \quad (2)$$

where λ = 2,4,6 abbreviates $^5D_0 \rightarrow {}^7F_\lambda$ transitions, and U^λ are the squared reduced matrix elements with values of 0.0032, 0.0023, and 0.0002 for λ = 2,4,6, respectively. ν is the emission barycenter energy, n is the refractive index, and I are the integrated emission intensities (the employed *MD* transition here is $^5D_0 \rightarrow {}^7F_1$). Equation (2) is given for intensities measured in counts. In the case where intensities are given in power units, the power to the ratio of barycenter energies should be equal to 4 [47].

From the Judd–Ofelt parameters, many derived quantities can be estimated directly: radiative transition probabilities, branching ratios, radiative lifetime, and emission cross-sections [48]. The radiative transition probabilities for a given λ and MD transition are given by Equations (3) and (4), respectively [49]:

$$A_\lambda \left[\mathrm{s}^{-1}\right] = 8.034 \times 10^9 \nu_\lambda^3 n_\lambda \left(n_\lambda^2+2\right)^2 U^\lambda \Omega_\lambda, \quad (3)$$

$$A_{MD} \left[\mathrm{s}^{-1}\right] = 3 \times 10^{-12} \nu_{MD}^3 n_{MD}^3, \quad (4)$$

The radiative lifetime, branching ratios, and emission cross-sections are estimated by Equations (5)–(7), respectively [50,51]:

$$\tau_{rad}[\mathrm{ms}] = \frac{10^3}{\sum_{\lambda=2,4,6} A_\lambda[s^{-1}] + A_{MD}[s^{-1}]}, \quad (5)$$

$$\beta_{\lambda,MD} = 10^{-3} A_{\lambda,MD} \left[\mathrm{s}^{-1}\right] \tau_{rad}[\mathrm{ms}], \quad (6)$$

$$\sigma_{\lambda,MD} \left[\mathrm{cm}^2\right] = \frac{1.33 \times 10^{-5}}{\nu_{\lambda,MD}^4 n_{\lambda,MD}^2} \frac{\max i_{\lambda,MD}}{I_{\lambda,MD}} A_{\lambda,MD}, \quad (7)$$

where max(i) is the intensity at the transition maximum.

The experimentally measured lifetime values (τ_{obs}) of the emissions from the $^5D_0$ level are given in Table 3, allowing for the calculation of the non-radiative lifetime (τ_{NR}) by [52]:

$$\tau_{NR}[\mathrm{ms}] = \frac{\tau_{rad}\tau_{obs}}{\tau_{rad} - \tau_{obs}}. \quad (8)$$

The Judd–Ofelt parameters and derived quantities were calculated by the JOES application software and are given in Table 3 [51]. With the increase of Y content in the hosts (increasing x), certain trends can be observed: the Ω_2 parameter of the hypersensitive transition $^5D_0 \rightarrow {}^7F_2$ increases with x, indicating an increasing degree of covalency and decrease of Eu^{3+} site symmetry, and the Ω_4 parameter, which relates to the viscosity and rigidity of the host matrix, shows no significant change [53]. The Ω_6 parameter could not be estimated, as the emission $^5D_0 \rightarrow {}^7F_6$ was not observed.

According to the changes in the refractive index and Judd–Ofelt parameters, the radiative transition probabilities and cross-sections show a monotonic increase with x, while the radiative lifetime decreases. As the observable lifetime also increases with x, the non-radiative lifetime is at a minimum in the pure $YNbO_4$, indicating that $LuNbO_4$ is a more efficient host matrix for the Eu^{3+} emission.

As the Judd–Ofelt parameters depend on the environment of the ion, the parameters obtained by the semi-empirical method are a statistical average of the Judd–Ofelt parameters for each ion. Thus, if there is a mix of non-equivalent sites in the host matrix,

the Judd–Ofelt parameters represent an average value for each site, weighted by their contribution [49]. Thus, the Judd–Ofelt parameters of the mixture of two hosts can be predicted from the Judd–Ofelt parameters of the two pure compounds (a,b):

$$\Omega_\lambda = x\Omega_\lambda^{(a)} + (1-x)\Omega_\lambda^{(b)}. \quad (9)$$

Table 3. Judd–Ofelt parameters of $Y_xLu_{1-x}NbO_4:Eu^{3+}$, branching ratios (β), radiative lifetimes (τ_{rad}), emission cross-sections (σ), radiative transition probabilities (A), total radiative transition probabilities (A_R), observed lifetime (τ_{obs}), non-radiative lifetime (τ_{NR}), and intrinsic quantum yield (η_{int}). Transitions $^5D_0 \rightarrow {}^7F_{1,2,4}$ are abbreviated with MD, 2, and 4 in subscripts, respectively.

x	0	0.25	0.50	0.75	1
$\Omega_2 \cdot 10^{20}$ [cm^2]	6.75	6.88	7.37	7.41	7.48
$\Omega_4 \cdot 10^{20}$ [cm^2]	2.69	2.91	2.97	3.01	2.95
β_{MD} [%]	14	14	14	14	14
β_2 [%]	73	73	73	73	73
β_4 [%]	13	14	14	14	13
τ_{rad} [ms]	0.782	0.859	0.916	1.027	1.134
$\sigma_{MD} \cdot 10^{21}$ [cm^2]	2.12	1.81	1.64	1.43	1.49
$\sigma_2 \cdot 10^{21}$ [cm^2]	9.96	9.40	9.71	9.01	8.87
$\sigma_4 \cdot 10^{21}$ [cm^2]	3.63	3.50	3.64	3.13	3.18
A_{MD} [s^{-1}]	179	163	148	133	120
A_2 [s^{-1}]	928	838	795	705	628
A_4 [s^{-1}]	171	164	148	136	115
A_R [s^{-1}]	1279	1164	1092	974	882
τ_{obs} [ms]	0.619	0.643	0.650	0.650	0.652
τ_{NR} [ms]	2.970	2.557	2.238	1.771	1.534
η_{int} [%]	79	75	71	63	57

The estimation of the Judd–Ofelt parameters from the emission spectra inherently brings an error of about 10%. By fitting the Judd–Ofelt parameters to the linear relations for each x, the Judd–Ofelt parameters can be refined by the values on the fitted curve, as the estimate reduces the error of estimation for each by $\sqrt{k}$, where k is the number of measurements. Thus, in the case of the mixture of $YNbO_4$ and $LuNbO_4$ in five ratios, the error of each estimated Judd–Ofelt parameter is reduced about 2.2 times, and the more correct values are on the fitted curve for each concentration (Figure 5).

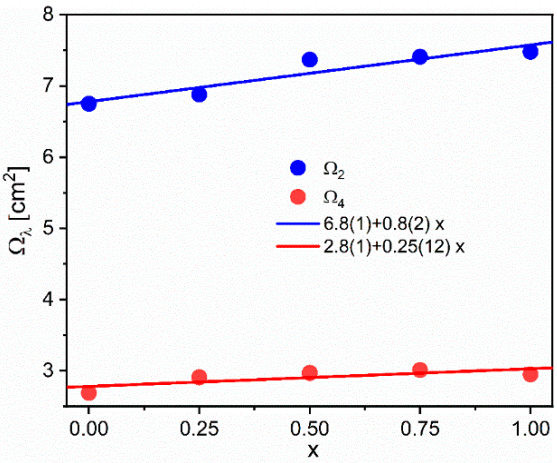

Figure 5. Experimentally obtained Judd–Ofelt parameters and corresponding linear fits.

4. Conclusions

In this study, we demonstrated how the Y-to-Lu ratio in $Y_xLu_{1-x}NbO_4$:Eu^{3+} powder material influenced the Eu^{3+} luminescence features. The materials were synthesized using the solid state reaction method. All of the structures crystallized as beta-Fergusonite, in which the Eu ion replaced the Y or Lu ion in a large, low-symmetry octahedron. In all composition hosts, the luminescence excitation and emission spectra of the Eu^{3+} ($4f^6$) ion showed characteristic *f-f* transitions from which the Stark energy levels were calculated.

The specific features and energy positions of the characteristic $^5D_0 \rightarrow {}^7F_1$ magnetic dipole transition were determined when measured with a higher resolution and when spectra deconvolution was used. The maximum ΔE splitting of the Stark splitting of $^7F_1$ manifold and the asymmetry ratio R all exhibit Y/Lu content-dependent trends. Calculations based on the Judd–Ofelt theory were used to estimate specific quantities, concluding that $LuNbO_4$ is a more efficient host matrix for the Eu^{3+} emission.

Author Contributions: Conceptualization, V.Đ. and M.D.D.; methodology, M.D.D.; validation, A.Ć.; formal analysis, A.Ć. and V.Đ.; investigation, M.S. and T.D.; data curation, L.Đ.F. and A.Ć.; writing—original draft preparation, V.Đ.; writing—review and editing, V.Đ., A.Ć. and M.D.D. All authors have read and agreed to the published version of the manuscript.

Funding: This research was funded by the NATO Science for Peace and Security Programme under grant id. [G5751]. The authors acknowledge funding from the Ministry of Education, Science and Technological Development of the Republic of Serbia.

Institutional Review Board Statement: Not applicable.

Informed Consent Statement: Not applicable.

Data Availability Statement: Not applicable.

Acknowledgments: The authors acknowledge Đorđe Veljović for SEM measurements.

Conflicts of Interest: The authors declare no conflict of interest.

References

1. Yen, W.M.; Shionoya, S.; Yamamoto, H. (Eds.) *Practical Applications of Phosphors*; CRC Press: Boca Raton, FL, USA, 2007; ISBN 9781315219974. [CrossRef]
2. Atuchin, V.V.; Subanakov, A.K.; Aleksandrovsky, A.S.; Bazarov, B.G.; Bazarova, J.G.; Gavrilova, T.A.; Krylov, A.S.; Molokeev, M.S.; Oreshonkov, A.S.; Stefanovich, S.Y. Structural and spectroscopic properties of new noncentrosymmetric self-activated borate $Rb_3EuB_6O_{12}$ with B_5O_{10} units. *Mater. Des.* **2018**, *140*, 488–494. [CrossRef]
3. Atuchin, V.V.; Aleksandrovsky, A.S.; Chimitova, O.D.; Gavrilova, T.A.; Krylov, A.S.; Molokeev, M.S.; Oreshonkov, A.S.; Bazarov, B.G.; Bazarova, J.G. Synthesis and spectroscopic properties of monoclinic α-$Eu_2(MoO_4)_3$. *J. Phys. Chem. C* **2014**, *118*, 15404–15411. [CrossRef]
4. Shi, P.; Xia, Z.; Molokeev, M.S.; Atuchin, V.V. Crystal chemistry and luminescence properties of red-emitting $CsGd_{1-x}Eu_x(MoO_4)_2$ solid-solution phosphors. *Dalton Trans.* **2014**, *43*, 9669–9676. [CrossRef] [PubMed]
5. Binnemans, K. Interpretation of europium(III) spectra. *Coord. Chem. Rev.* **2015**, *295*, 1–45. [CrossRef]
6. Tanner, P.A. Some misconceptions concerning the electronic spectra of tri-positive europium and cerium. *Chem. Soc. Rev.* **2013**, *42*, 5090. [CrossRef]
7. Đorđević, V.; Antić, Ž.; Lojpur, V.; Dramićanin, M.D. Europium-doped nanocrystalline $Y_2O_3-La_2O_3$ solid solutions with bixbyite structure. *J. Phys. Chem. Solids* **2014**, *75*, 1152–1159. [CrossRef]
8. Đorđević, V.; Antić, Ž.; Nikolić, M.G.; Dramićanin, M.D. Comparative structural and photoluminescent study of Eu^{3+}-doped La_2O_3 and $La(OH)_3$ nanocrystalline powders. *J. Phys. Chem. Solids* **2014**, *75*, 276–282. [CrossRef]
9. Blasse, G.; Bril, A. Luminescence of Phosphors Based on Host Lattices ABO_4 (A is Sc, In; B is P, V, Nb). *J. Chem. Phys.* **2003**, *50*, 2974. [CrossRef]
10. Ding, S.; Zhang, H.; Liu, W.; Sun, D.; Zhang, Q. Experimental and first principle investigation the electronic and optical properties of $YNbO_4$ and $LuNbO_4$ phosphors. *J. Mater. Sci. Mater. Electron.* **2018**, *29*, 11878–11885. [CrossRef]
11. Rubin, J.J.; Van Uitert, L.G. Growth of Large Yttrium Vanadate Single Crystals for Optical Maser Studies. *J. Appl. Phys.* **1966**, *37*, 2920. [CrossRef]
12. Erdei, S. Growth of oxygen deficiency-free YVO_4 single crystal by top-seeded solution growth technique. *J. Cryst. Growth* **1993**, *134*, 1–13. [CrossRef]

13. Packer, R.J.; Tsipis, E.V.; Munnings, C.N.; Kharton, V.V.; Skinner, S.J.; Frade, J.R. Diffusion and conductivity properties of cerium niobate. *Solid State Ion.* **2006**, *177*, 2059–2064. [CrossRef]
14. Haugsrud, R.; Norby, T. Proton conduction in rare-earth ortho-niobates and ortho-tantalates. *Nat. Mater.* **2006**, *5*, 193–196. [CrossRef]
15. Wu, M.; Liu, X.; Gu, M.; Ni, C.; Liu, B.; Huang, S. Characterization and luminescence properties of sol–gel derived M′-type $LuTaO_4$:Ln^{3+} (Ln = Pr, Sm, Dy) phosphors. *Mater. Res. Bull.* **2014**, *60*, 652–658. [CrossRef]
16. Takei, H.; Tsunekawa, S. Growth and properties of $LaNbO_4$ and $NdNbO_4$ single crystals. *J. Cryst. Growth* **1977**, *38*, 55–60. [CrossRef]
17. Fulle, K.; McMillen, C.D.; Sanjeewa, L.D.; Kolis, J.W. Hydrothermal Chemistry and Growth of Fergusonite-type $RENbO_4$ (RE = La-Lu, Y) Single Crystals and New Niobate Hydroxides. *Cryst. Growth Des.* **2016**, *16*, 4910–4917. [CrossRef]
18. Brunckova, H.; Mudra, E.; Medvecky, L.; Kovalcikova, A.; Durisin, J.; Sebek, M.; Girman, V. Effect of lanthanides on phase transformation and structural properties of $LnNbO_4$ and $LnTaO_4$ thin films. *Mater. Des.* **2017**, *134*, 455–468. [CrossRef]
19. Zhang, P.; Wang, T.; Xia, W.; Li, L. Microwave dielectric properties of a new ceramic system $NdNbO_4$ with CaF_2 addition. *J. Alloys Compd.* **2012**, *535*, 1–4. [CrossRef]
20. Đačanin, L.R.; Dramićanin, M.D.; Lukić-Petrović, S.R.; Petrović, D.M.; Nikolić, M.G.; Ivetić, T.B.; Gúth, I.O. Mechanochemical synthesis of $YNbO_4$:Eu nanocrystalline powder and its structural, microstructural and photoluminescence properties. *Ceram. Int.* **2014**, *40*, 8281–8286. [CrossRef]
21. Blasse, G.; Bril, A. Photoluminescent Efficiency of Phosphors with Electronic Transitions in Localized Centers. *J. Electrochem. Soc.* **1968**, *115*, 1067. [CrossRef]
22. Lee, S.K.; Chang, H.; Han, C.H.; Kim, H.J.; Jang, H.G.; Park, H.D. Electronic Structures and Luminescence Properties of $YNbO^4$ and $YNbO^4$:Bi. *J. Solid State Chem.* **2001**, *156*, 267–273. [CrossRef]
23. Dwivedi, A.; Mishra, K.; Rai, S.B. Tm^{3+}, Yb^{3+} activated $ANbO_4$ (A = Y, Gd, La) phosphors: A comparative study of optical properties (downshifting and upconversion emission) and laser induced heating effect. *J. Phys. D Appl. Phys.* **2016**, *50*, 045602. [CrossRef]
24. Xiao, X.; Yan, B. $REMO_4$ (RE = Y, Gd; M = Nb, Ta) phosphors from hybrid precursors: Microstructure and luminescence. *J. Mater. Res.* **2008**, *23*, 679–687. [CrossRef]
25. Liu, C.; Zhou, W.; Shi, R.; Lin, L.; Zhou, R.; Chen, J.; Li, Z.; Liang, H. Host-sensitized luminescence of Dy^{3+} in $LuNbO_4$ under ultraviolet light and low-voltage electron beam excitation: Energy transfer and white emission. *J. Mater. Chem. C* **2017**, *5*, 9012–9020. [CrossRef]
26. Dačanin, L.R.; Lukić-Petrović, S.R.; Petrović, D.M.; Nikolić, M.G.; Dramićanin, M.D. Temperature quenching of luminescence emission in Eu^{3+}- and Sm^{3+}-doped $YNbO_4$ powders. *J. Lumin.* **2014**, *151*, 82–87. [CrossRef]
27. Wang, X.; Li, X.; Xu, S.; Cheng, L.; Sun, J.; Zhang, J.; Li, L.; Chen, B. A comparative study of spectral and temperature sensing properties of Er^{3+} mono-doped $LnNbO_4$ (Ln = Lu, Y, Gd) phosphors under 980 and 1500 nm excitations. *Mater. Res. Bull.* **2019**, *111*, 177–182. [CrossRef]
28. Ding, S.; Peng, F.; Zhang, Q.; Luo, J.; Liu, W.; Sun, D.; Dou, R.; Sun, G. Structure, spectroscopic properties and laser performance of Nd:$YNbO_4$ at 1066 nm. *Opt. Mater.* **2016**, *62*, 7–11. [CrossRef]
29. Massabni, A.M.G.; Montandon, G.J.M.; Couto, M.A.; Santos, D. Synthesis and luminescence spectroscopy of $YNbO_4$ doped with Eu(III). *Mater. Res.* **1998**, *1*, 01–04. [CrossRef]
30. Đačanin Far, L.; Lukić-Petrović, S.R.; Đorđević, V.; Vuković, K.; Glais, E.; Viana, B.; Dramićanin, M.D. Luminescence temperature sensing in visible and NIR spectral range using Dy^{3+} and Nd^{3+} doped $YNbO_4$. *Sens. Actuators A Phys.* **2018**, *270*, 89–96. [CrossRef]
31. Refguson, R.B. The crystallography of synthetic $YTaO_4$ and fused fergusonite | The Canadian Mineralogist | GeoScienceWorld. *Can. Mineral.* **1957**, *6*, 72–77.
32. Brixner, L.H.; Whitney, J.F.; Zumsteg, F.C.; Jones, G.A. Ferroelasticity in the $LnNbO_4$-type rare earth niobates. *Mater. Res. Bull.* **1977**, *12*, 17–24. [CrossRef]
33. Bayliss, R.D.; Pramana, S.S.; An, T.; Wei, F.; Kloc, C.L.; White, A.J.P.; Skinner, S.J.; White, T.J.; Baikie, T. Fergusonite-type $CeNbO_{4+\delta}$: Single crystal growth, symmetry revision and conductivity. *J. Solid State Chem.* **2013**, *204*, 291–297. [CrossRef]
34. Arulnesan, S.W.; Kayser, P.; Kimpton, J.A.; Kennedy, B.J. Studies of the fergusonite to scheelite phase transition in $LnNbO_4$ orthoniobates. *J. Solid State Chem.* **2019**, *277*, 229–239. [CrossRef]
35. Keller, C. Über ternäre Oxide des Niobs und Tantals vom Typ ABO_4. *Z. Anorg. Allg. Chem.* **1962**, *318*, 89–106. [CrossRef]
36. Weitzel, H. Kristallstrukturverfeinerungen von Euxenit, $Y(Nb_{0.5}Ti_{0.5})_2O_6$, und M-Fergusonit, $YNbO_4$. *Z. Krist.-Cryst. Mater.* **1980**, *152*, 69–82. [CrossRef]
37. Shannon, R.D. Revised effective ionic radii and systematic studies of interatomic distances in halides and chalcogenides. *Acta Crystallogr. Sect. A* **1976**, *32*, 751–767. [CrossRef]
38. Malta, O.L.; Antic-Fidancev, E.; Lemaitre-Blaise, M.; Milicic-Tang, A.; Taibi, M. The crystal field strength parameter and the maximum splitting of the $^7F_1$ manifold of the Eu^{3+} ion in oxides. *J. Alloys Compd.* **1995**, *228*, 41–44. [CrossRef]
39. Görller-Walrand, C.; Binnemans, K. Chapter 155 Rationalization of crystal-field parametrization. *Handb. Phys. Chem. Rare Earths* **1996**, *23*, 121–283. [CrossRef]

40. Srivastava, A.M.; Brik, M.G.; Beers, W.W.; Cohen, W. The influence of nd^0 transition metal cations on the Eu^{3+} asymmetry ratio R = $I(^5D_0-{}^7F_2)/I(^5D_0-{}^7F_1)$ and crystal field splitting of $^7F_1$ manifold in pyrochlore and zircon compounds. *Opt. Mater.* **2021**, *114*, 110931. [CrossRef]
41. Görller-Walrand, C.; Fluyt, L.; Ceulemans, A.; Carnall, W.T. Magnetic dipole transitions as standards for Judd-Ofelt parametrization in lanthanide spectra. *J. Chem. Phys.* **1991**, *95*, 3099–3106. [CrossRef]
42. Ćirić, A.; Stojadinović, S.; Brik, M.G.; Dramićanin, M.D. Judd-Ofelt parametrization from emission spectra: The case study of the Eu^{3+} $^5D_1$ emitting level. *Chem. Phys.* **2020**, *528*, 110513. [CrossRef]
43. Judd, B.R. Optical Absorption Intensities of Rare-Earth Ions. *Phys. Rev.* **1962**, *127*, 750–761. [CrossRef]
44. Ofelt, G.S. Intensities of Crystal Spectra of Rare-Earth Ions. *J. Chem. Phys.* **1962**, *37*, 511–520. [CrossRef]
45. Ćirić, A.; Stojadinović, S.; Dramićanin, M.D. An extension of the Judd-Ofelt theory to the field of lanthanide thermometry. *J. Lumin.* **2019**, *216*. [CrossRef]
46. Babu, S.S.; Babu, P.; Jayasankar, C.K.; Sievers, W.; Tröster, T.; Wortmann, G. Optical absorption and photoluminescence studies of Eu^{3+}-doped phosphate and fluorophosphate glasses. *J. Lumin.* **2007**, *126*, 109–120. [CrossRef]
47. Suta, M.; Meijerink, A. A Theoretical Framework for Ratiometric Single Ion Luminescent Thermometers—Thermodynamic and Kinetic Guidelines for Optimized Performance. *Adv. Theory Simul.* **2020**, *3*, 2000176. [CrossRef]
48. Hehlen, M.P.; Brik, M.G.; Krämer, K.W. 50th anniversary of the Judd–Ofelt theory: An experimentalist's view of the formalism and its application. *J. Lumin.* **2013**, *136*, 221–239. [CrossRef]
49. Görller-Walrand, C.; Binnemans, K. Chapter 167 Spectral intensities of f-f transitions. *Handb. Phys. Chem. Rare Earths* **1998**, *25*, 101–264.
50. Babu, P.; Jayasankar, C.K. Optical spectroscopy of Eu^{3+} ions in lithium borate and lithium fluoroborate glasses. *Phys. B Condens. Matter* **2000**, *279*, 262–281. [CrossRef]
51. Ćirić, A.; Stojadinović, S.; Sekulić, M.; Dramićanin, M.D. JOES: An application software for Judd-Ofelt analysis from Eu^{3+} emission spectra. *J. Lumin.* **2019**, *205*, 351–356. [CrossRef]
52. Dramićanin, M.D. Sensing temperature via downshifting emissions of lanthanide-doped metal oxides and salts. A review. *Methods Appl. Fluoresc.* **2016**, *4*, 042001. [CrossRef] [PubMed]
53. Brik, M.G.; Antic, Ž.M.; Vuković, K.; Dramićanin, M.D. Judd-Ofelt Analysis of Eu^{3+} Emission in TiO_2 Anatase Nanoparticles. *Mater. Trans.* **2015**, *56*, 1416–1418. [CrossRef]